Coordination Chemistry Reviews, 65 (1985) 285–307
Elsevier Science Publishers B.V., Amsterdam – Printed in The Netherlands

X-RAY DIFFRACTION AND THE CHARGE DISTRIBUTION IN TRANSITION METAL COMPLEXES

PHILIP COPPENS

Department of Chemistry, State University of New York at Buffalo, Buffalo, NY 14214 (U.S.A.)

(Received 25 October 1984)

CONTENTS

A. INTRODUCTION

It is hardly necessary to point out that electrons play a pivotal part in determining the nature and properties of transition metal complexes. Methods to obtain the electron distribution are therefore of importance. The distribution can be calculated theoretically or measured experimentally, in particular with X-ray scattering techniques. However, both methods have specific drawbacks. In theoretical calculations of large complexes, computational shortcuts are often necessary, in particular in the evaluation of four-center integrals and the size of the atomic orbital basis set. On the other hand, experimental densities are sensitive to systematic measurement errors and require very careful experimentation.

The effects of such limitations are very different for the two methods and affect different regions of space. For example, several experimental effects combine to produce large uncertainties in the charge density close to the nuclei of heavier atoms, while the theoretical method, being an energy minimization procedure, is likely to be most reliable exactly in these regions where the electron energy has a large magnitude. On the other hand, basis

0010-8545/85/$08.05

set truncation in theoretical calculations has a pronounced effect on the resulting bond and lone pair densities. Such arguments suggest that theoretical and experimental methods are complementary and that combined application may be a most fruitful approach.

However, this comparison is complicated by the fact that the experimental results necessarily refer to the vibrating molecule while the theoretical calculations are done on the static entity, which is not an experimental observable. For small molecules methods have been developed for the smearing of the theoretical density over the rigid body molecular motions. These have much larger amplitudes than the internal modes for molecules such as formamide or oxalic acid to which this thermal smearing procedure has been applied.

More complex molecules are much less rigid and may have segments with relatively large thermal displacements. This means that the thermal smearing is more difficult as it requires detailed knowledge of the molecular mechanics. An alternative is the use of a model to separate thermal motion smearing from the effects of bonding in the experimental distribution. One such model is described below. After fitting of the model to the observed intensities, the electron distribution based on the parametrized model functions may be plotted. The resulting distribution is to some extent dependent on the completeness and the nature of the model functions. For this reason comparison of theory and experiment for more complex molecules is usually qualitative, i.e. general features such as nature and position of peaks and valleys are compared, rather than peak heights and trough depths. In any case it is advisable to perform the experiment at low temperature, in order to minimize thermal smearing as much as possible.

The accurate X-ray diffraction intensities, used in the experimental method, are in some studies combined with neutron data [1], from which atomic positions unbiased by bonding are obtained. This is especially important when the electron density in the vicinity of hydrogen atoms is to be studied.

A number of publications containing surveys of the field are available [2–4]. A less well-known complementary technique, based on the interaction of polarized neutrons with the magnetic moment of the electrons, allows the determination of the spin density in paramagnetic materials [5]. Combination of the charge and spin density should give an unusually detailed picture of bonding in such materials, but has only been attempted in very few cases so far (see for example refs. 46 and 47).

This review summarizes a number of pertinent concepts and gives several examples of their application, including studies of transition metal carbonyls, metalloporphyrins, metal–metal and metal–ligand bonding.

B. DEFORMATION MAPS: WHAT TO SUBTRACT TO VISUALIZE CHEMICAL BONDING

Since the map of the total electron distribution is dominated by the accumulation of electrons near the nuclei, it is not a suitable choice for illustration of the influence of molecule formation on the charge distribution. On the other hand, the total density can very well be interpreted in terms of molecular structure and its change in chemical processes. A theory based on the topology of the total electron distribution, has been used with much success by Bader and coworkers [6].

In order to demonstrate the deformation of the density upon the bonding of atoms to form a molecule, subtraction of the hypothetical distribution which would exist prior to bond formation is most informative. A fundamental definition for this reference state is that of the *promolecule*, the superposition of ground state spherical atoms positioned according to the molecular geometry. The corresponding function:

$$\Delta\rho = \rho_{\text{total}} - \rho_{\text{spherical atoms}}$$

is commonly referred to as the *deformation density* or *atom deformation density* [7]. It describes the deformation of the charge density due to forces between atoms. This effect is completely neglected in the structure factor formalism used in conventional crystallographic work.

If we are specifically interested in bonding between particular fragments of a molecule we may use the *fragment deformation density* obtained by subtracting fragment densities from the total molecular distribution. In the case of a transition metal complex, such a fragment may be a metal atom plus ligand, or some other part of the complex, or it may be the isolated ligand, in which case we will use the term *ligand deformation density*.

In the experimental study of nonacarbonyl-μ_3-methylidyne-triangulocobalt ($Co_3CH(CO)_9$) by Leung [8], the CH fragment density was calculated theoretically (Fig. 1a), thermally smeared to allow for vibrational effects, and subtracted from the experimental density. The fragment deformation map shows deficiency in the σ-region and excess in the π-region (Fig. 2a), both resulting from the metal–ligand bonding. The atom deformation map (Fig. 2b) on the other hand is dominated by the overlap density in the carbon hydrogen bond and the lone pair density on the carbon atom.

The CH radical has a low-lying $^4\Sigma$ excited state, in which one of the σ electrons is excited to a π level (Fig. 1c). Subtraction of this excited fragment from the experimental density removes the excess π charge, but not the lone pair density on the carbon atom (Fig. 2c). The electron distribution in the bonded ligand is apparently intermediate between the densities of the ground and first excited state of the isolated fragment.

A metal-atom containing fragment was subtracted in a series of theoretical studies by Hall [9]. For nonacarbonyl-μ_3-chloromethylidyne-triangulocobalt, $Co_3CCl(CO)_9$, Hall's fragment deformation density is obtained by subtraction of three "prepared" $Co(CO)_3$ fragments. We may consider the formation of this complex to consist of two steps. Bonding of the carbonyls to the metal atom causes a decrease of density in the regions in which metal–metal bonds appear upon complex formation. This electron density is restored by metal–metal bonding. The two effects cancel in the atom deformation map. But the fragment deformation map, which only represents the effect of the second step shows density between the cobalt atoms. In addition it may be noted that covalent bonds between atoms with more than half-filled shells, such as oxygen and fluorine, do not show density accumu-

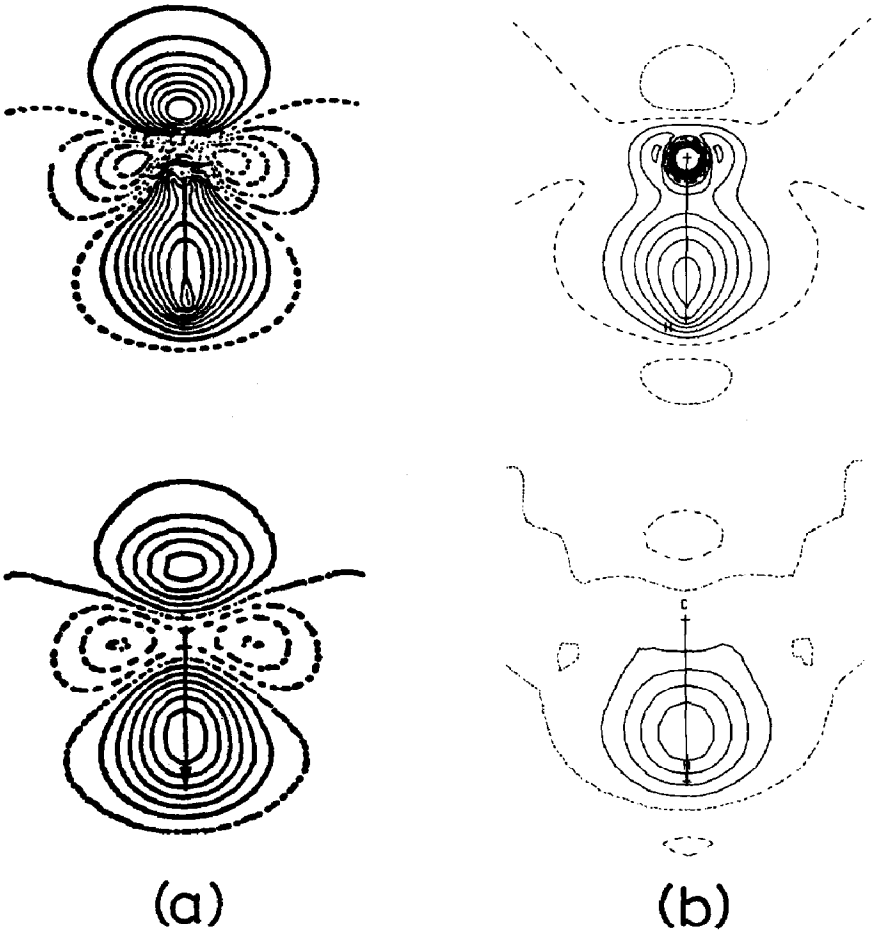

Fig. 1. Electron deformation densities of the CH radical. (a) $^2\Pi$ Ground state. Top, at rest; bottom: thermally smeared using experimental vibrational parameters. Contours: 0.1 eÅ^{-3} (b) $^4\Sigma$ Excited state. Top, at rest; bottom, thermally smeared using experimental vibrational parameters. Contours as in (a). From ref. 8.

Fig. 2. Deformation maps of CH ligand in $Co_3CH(CO)_9$. Contours as in Fig. 1. (a) Fragment deformation map subtracting $^2\Pi$ density. (b) Atom deformation map. (c) Fragment deformation map subtracting $^4\Sigma$ density. From ref. 8.

lation in the overlap regions because of the large number of electrons already in these regions in the promolecule. Subtraction of a "prepared" atom in such cases is analogous to subtracting a fragment of a complex, and leads to a function which shows overlap density.

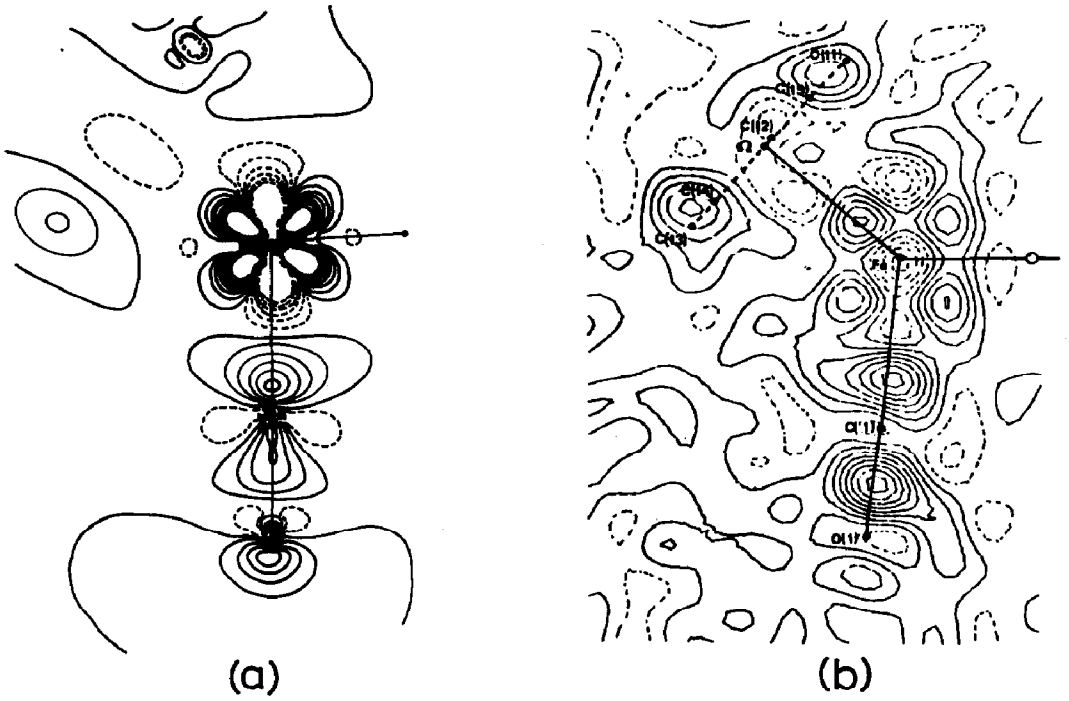

Fig. 3. Deformation density distribution in *trans*-[π-C_5H_5)Fe$(CO)_2]_2$ from ref. 12. Section containing Fe–Fe line and the terminal carbonyls. (a) Theoretical, contour interval 0.2 eÅ^{-3}. Dashed contours negative. (b) Experimental, contour interval 0.1 eÅ^{-3}. Broken contours negative.

This is one of the main causes of the generally observed absence of density accumulation in metal–metal bonds in atom deformation maps.

Theoretical atom deformation maps are in agreement with this observation. They have been calculated for a number of other complexes including chromiumtetracarboxylate [10], $Cr_2(HCOO)_4$, bis(dicarbonyl-π-cyclopentadienyliron) [11,12], $[C_5H_5Fe(CO)_2]_2$, and $Mn_2(CO)_{10}$ [13]. Only when metal–metal bonding is unusually strong will it dominate the atom deformation map, as is the case for the "supershort" Cr–Cr bond of 1.879 Å length, investigated recently and further discussed below.

An example of the good qualitative agreement that is obtained in the most careful studies is given in Fig. 3 [12]. The calculated and experimental atom deformation maps in a section through *trans*-$[\pi$-$(C_5H_5)Fe(CO)_2]_2$ show very similar features even without allowance for thermal smearing. The absence of density in the Fe–Fe bond is observed on the line to the right of the Fe atom which represents a bond across the molecular symmetry element. Other features in both maps are around the Fe atom (due to "intraorbital transfer" on complex formation), in the C–O bond, and in the lone pair regions near the C and O atoms. The experimental and theoretical maps in this section and in other sections not reproduced here, have been described as "topologically equivalent" [12].

C. ANALYTICAL DESCRIPTION OF THE CHARGE DENSITY: MULTIPOLES, *d*-ORBITALS AND THEIR INTERRELATION

It is common practice in X-ray structure determination to describe the molecular electron density as an assembly of isolated atom densities, the "promolecule", discussed above. However, the deformation maps show convincingly that this formalism is not adequate for high-quality data. A more sophisticated X-ray scattering model is needed to allow application of least-squares methods for the quantitative description of the charge distribution. Such a model must describe the charge transfer between atoms, the change in radial dependence of the charge density due to changes in screening of the nucleus, and the lack of spherical symmetry of the density around each atom. The first two effects may be allowed for by separating the core and valence shell densities and incorporating two parameters, P and κ, representing the valence shell population and its radial dependence respectively [14]

$$\rho_{\text{atom}}(r) = \rho_{\text{core}}(r) + P_{\text{valence}}\kappa^3\rho(\kappa r) \tag{1}$$

To allow for the asphericity of the atoms, expression (1) can be complemented by an expansion of atom-centered spherical harmonic functions.

$$\rho_{\text{atom}}(r) = \rho_{\text{core}}(r) + P_{\text{valence}}\kappa^3\rho(\kappa r) + \sum_l \sum_m P_{lm\pm} y_{lm\pm}(\theta, \phi) R_{lm}(r) \tag{2}$$

here the $y_{lm\pm}$ are real spherical harmonic functions, akin to the hydrogenic s, p and d orbitals, but defined as density functions, rather than as wavefunctions. The terms for $l = 1, 2, 3, 4$ correspond respectively to the dipolar, quadrupolar, octapolar and hexadecapolar components of the atomic charge density. The function $R_{lm}(r)$ describes the dependence of the density function y_{lm} on the distance from the atomic nucleus. Other analytical representations have been used, but it appears that eqn. (2), or closely related expressions [15], provide an adequate description of the various parts of the molecular density without introduction of redundant variables.

Though eqn. (2) does not explicitly allow for overlap density in the bonds, as all terms are atom-centered, the terms with large l are sufficiently diffuse to be able to represent this charge density. In trigonal or tetrahedral bonding geometries, common in carbon atom frameworks, bond overlap density is effectively represented by the octapolar ($l = 3$) terms, which have maxima in the appropriate directions. For transition metal atoms overlap density in bonds with ligands is generally small, so that the atomic approximation represented by eqn. (2) is more closely valid. It is therefore possible to relate the occupancy of the multipoles to the occupancy of the d-orbitals and products of d-orbitals, with occupancy P_i and P_{ij}, respectively

$$\rho_d(r) = \sum_{i=1}^{5} P_i d_i^2 + \sum_{i=1}^{5} \sum_{j>1}^{5} P_{ij} d_i d_j \tag{3}$$

The d-orbital functions are again spherical harmonic functions $y_{lm\pm}(\theta, \phi)$ multiplied by a radial dependence term, but with the normalization $\int \psi^2 d\tau = 1$, which is different from the normalization $\int |\psi| d\tau = 2$ for $l > 1$, and $\int |\psi| d\tau = 1$ for $l = 0$, used for the density functions [16]. The products of spherical harmonics occurring in eqn. (3) can be written as a linear combination of spherical harmonics, using the well-known Clebsch–Gordon coefficients [17]. Since the valence density parts of expressions (2) and (3) are formally equivalent, a linear relation can be derived between the multipole and the orbital populations, taking into account the differences in normalization between the wavefunctions and the density functions. Examples of these relations for O_h and D_{4h} point groups are given in Table 1.

An example of an octahedral complex that has been analyzed in this way is chromium hexacarbonyl $Cr(CO)_6$. The analysis is based on accurate data from the study by Rees and Mitschler [18].

Two multipoles are symmetry-allowed for octahedral local symmetry. They are the spherical function y_{00} and the combination $y_{40} + 0.7403 y_{44+}$. Though the symmetry of the crystallographic site is lower than O_h no significant deviations from the molecular symmetry were evident in the analysis. Results are compared in Table 2 with those from a theoretical SCF

TABLE 1

Relation between d-orbital populations and least-squares multipole population parameters for square planar and octahedral complexes. The numbers in the table are coefficients C in the expression $P(d) = \Sigma C_m P(y_m)$ (from ref. 31)

Point group O_h	P_{00}	P_{40} [a]		
$P(e_g)$	0.4	2.79		
$P(t_{2g})$	0.6	−2.79		
Point group D_{4h}	P_{00}	P_{20}	P_{40}	P_{44+}
P_{20} (a_{1g})	0.200	1.039	1.396	0
P_{21+} (e_g)	0.200	0.520	−0.931	0
P_{21-}	0.200	0.520	−0.931	0
P_{22+} (b_{1g})	0.200	−1.040	0.232	1.570
P_{22-} (b_{2g})	0.200	−1.040	0.232	−1.570

[a] P_{40} is the coefficient of the function $y_{40} + 0.7403\ y_{44+}$ in the case of cubic point group symmetry.

calculation using the X-αexchange approximation [13]. The experimental results are almost independent of the inclusion of chromium 4s scattering, which indicates that the net charge on the transition metal is poorly

TABLE 2

(a) Orbital populations for $Cr(CO)_6$ (ref. 31)

	With 4s	Without 4s	Theoretical	Spherical atom
e_g	1.42(5)	1.37(7)	1.12	2
t_{2g}	3.40(5)	3.32(8)	3.26	3
Total d	4.82(9)	4.69(9)	4.38	5
4s	1	–	−0.085	1
$4p_x$	–	–	−0.011	–
$4p_y$	–	–	−0.011	–
$4p_z$	–	–	−0.011	–

(b) Relative populations of 3d orbitals in $Co(NH_3)_6^{3+}$, $Co(CN)_6^{3-}$, $Cr(CN)_6^{3-}$ and $Cr(CO)_6$

	$Co(NH_3)_6^{3+}$		$Co(CN)_6^{3-}$			$Cr(CN)_6^{3+}$			$Cr(CO)_6$	
	Exp. [a]	Exp. [b]	Exp. [b]	Theory [c]	Theory [d]	Exp. [a]	Theory [c]	Theory [d]	Exp. [e]	Theory [f]
a_g(%)	26.4	24.3	25.0	79.3	67.5	19.4	68.9	61.3	70.8	74.5
e_g(%)	49.6	52.2	49.2			49.9				
e'_g(%)	24.1	23.5	25.9	20.7	32.5	30.7	31.1	38.7	29.2	25.5

[a] Ref. 31, $Co(NH_3)_6Cr(CN)_6$. [b] Ref. 31 $Co(NH_3)_6Cr(CN)_6$. [c] Ref. 53, ab-initio SCF calculation. [d] Ref. 54, X-α calculation. [e] Refs. 18, 31. [f] Ref. 13, SCF with X-α exchange.

determined, unlike the asphericity of the atomic density. The preferential occcupancy of the t_{2g} (i.e. d_{xy}, d_{xz}, d_{yz}) orbitals is evident in both theory and experiment, and as expected from the splitting of the *d*-orbital levels in an octahedral field.

A similar effect is observed in the trigonally distorted complex ions in $Co(NH_3)_6Cr(CN)_6$ and $Co(NH_3)_6Co(CN)_6$, first studied by Iwata and Saito [19] and Iwata [20]. The *d*-orbital populations expressed as percentages of total number of *d*-electrons are given in Table 2b. In all cases the e'_g orbitals, which are directed towards the ligand atoms, are depopulated relative to the spherical atoms. The remaining non-zero population of these orbitals indicates σ-donation from the ligands as predicted by a covalent bonding scheme [21]. The e'_g population is larger for the hexa-cyano than for the metal hexamine complex ions, in agreement with accepted chemical concepts, which predict stronger covalent bonding for CN than for NH_3. The population of this type orbital appears to be considerably overestimated by the X-α calculations on the hexacyanide complexes, while the ab-initio results are much closer, both for the hexacyanides and for chromium hexacarbonyl.

It is further interesting to note that the $Cr(CN)_6^{3-}$ and $Cr(CO)_6$ *d*-orbital occupancies (listed in the last column) are the same, indicating a close similarity between the isoelectronic CN^- and CO ligands.

Other studies, in agreement with those described here, have been reported for pyrite [22], $KFeF_3$, $KNiF_3$, $KMnF_3$ [23] and in several other complexes.

Fe(II)phthalocyanine (FePc) [24] is an example of a D_{4h} complex, for which the electronic ground state is still not firmly established. Though FePc is clearly in an intermediate spin state with $S = 1$, several theoretical and experimental studies give conflicting results regarding the nature of the ground state configuration. It has been described as both ^3EA and ^3B, while for Fe(II)tetraphenylporphyrin (FeTPP) a ^3A state has also been deduced (see Table 3 for definition of the configurations). The *d*-orbital populations obtained from the experimental multipole populations are close to those for the ^3EA ground state and not compatible with the ^3A or ^3B configurations (Table 3). The deficiency of density in the d_{z^2} orbital may be a result of the packing of the molecules in the solid, in which a nitrogen atom of an adjacent molecule is located along the axial coordination direction (z axis) at 3.343 Å from the iron atom. In the crystals of FeTPP, on the other hand, no such axial approach is found. Accordingly the d_{z^2} orbital is found to have a significantly larger population [25].

While for FePc a ratio of *d*-orbital occupancies $P(d_{z^2}) : P(d_{xz,yz}) : P(d_{xy})$ of 1.3 : 3 : 2.4 is found, the corresponding ratio for FeTPP is 1.7 : 3 : 1.3. Both complexes can be interpreted as having a ground state intermediate between ^3EA and ^3EB (see Table 3 for definitions), with a much larger admixture of

TABLE 3

Iron phthalocyanine: electron occupancies of several configurations and comparison with experimental results [a] (from ref. 24)

	^3E_gA	^3A_g	$^3B_{2g}$	^3E_gB
$d_{x^2-y^2}$	–	–	–	–
d_{z^2}	1(17%)	2(33%)	1(17%)	2(33%)
d_{xz}, d_{yz}	3(49%)	2(33%)	4(67%)	3(49%)
d_{xy}	2(33%)	2(33%)	1(17%)	1(17%)

	X-ray experimental	Spherical atom
$d_{x^2-y^2}$	0.70 (7) (12.9%)	1.2(20%)
d_{z^2}	0.93 (6) (17.1%)	1.2(20%)
d_{xz}, d_{yz}	2.12 (7) (39.1%)	2.4(40%)
d_{xy}	1.68 (10) (30.9%)	1.2(20%)

[a] The z axis is the four-fold symmetry axis perpendicular to the molecular plane. The x and y axes are in the plane along the Fe–N bonds.

^3EB in the case of FeTPP. While the energy levels are close, and theoretical conclusions therefore difficult, the configurations have very different electron density distributions and can be well distinguished experimentally. The experiment refers of course, to the solid state. The possibility of differences between solid-state and gas-phase electronic structure must be kept in mind.

Even more detailed information on the nature of paramagnetic transition metal complexes can be obtained by simultaneous analysis of charge and spin density results, as discussed further below.

D. NET CHARGES ON TRANSITION METAL ATOMS: CAN THEY BE DEFINED?

Use of expressions such as (1) and (2) in a least-squares procedure yields a set of charge density parameters which include the valence shell population P_{valence} and the population P_{00} of the y_{00} term in (2) (in our work the latter term is often omitted, because it is very similar to the valence term). Together with the nuclear and core electron charges these values yield the net charge on the atom in question. For light atoms such as carbon, nitrogen and oxygen very reasonable values are obtained, which lead to molecular dipole moments in good agreement with literature values from other physico-chemical methods. Such X-ray solid-state dipole moments are available for formamide [26], glycylglycine [27], sulfamic acid [28], pyridinium 1-dicyanomethylide [29], 2′-deoxycytidine 5′-monophosphate [30], and a number of other compounds.

For a transition metal complex the analysis is hampered by the very diffuse nature of the outer *s*-electron distribution, which only contributes to X-ray scattering at very low values of sin θ/λ. That is why the least-squares results for $Cr(CO)_6$ (Table 2) and a series of other transition metal complexes [31] are hardly affected by the inclusion of the 4*s*-electrons in the scattering formalism.

If the least-squares method is ambiguous, would it be possible to use the electron density directly and count the electrons in a well-defined volume assigned to each of the atoms?

Figure 4 shows the radial distribution $4\pi r^2\psi^2$ as a function of distance from the nucleus for the 3*d* and 4*s* electrons of an isolated chromium atom. Since the Cr–C distance in chromium-hexacarbonyl is 1.90 Å, it can be seen that most of the metal atom's 4*s* density is closer to the ligand than to the

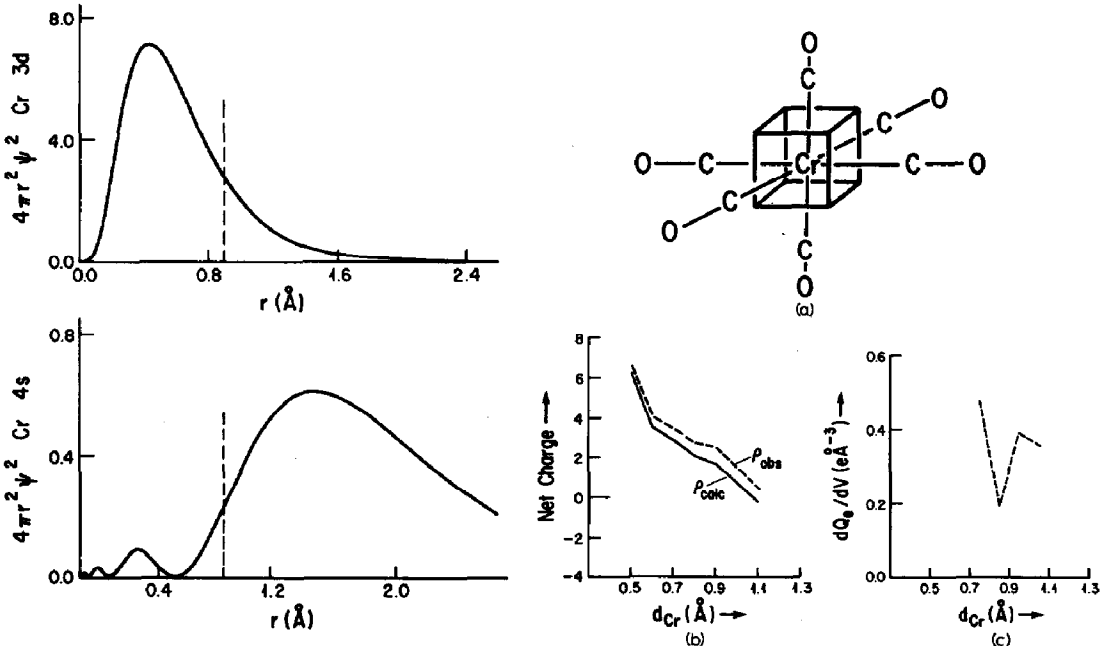

Fig. 4. Radial probability distribution function vs. distance from the nucleus for the isolated chromium atom. Top, 3*d* electrons; bottom, 4*s* electrons. The vertical lines indicate the boundary selected for $Cr(CO)_6$ by the condition that the average electron density on the polyhedral surface be a minimum as a function of distance. From ref. 33.

Fig. 5. (a) Polyhedral volume of integration for $Cr(CO)_6$. (b) Net charge on Cr in $Cr(CO)_6$ versus d_{Cr}, the distance of the boundary plane from the chromium atom. Obs: from X-ray data. Calc: superposition of spherical atoms with X-ray thermal motion. (c) Average charge on the polyhedral surface of the chromium atom as a function of d_{Cr}. From ref. 33.

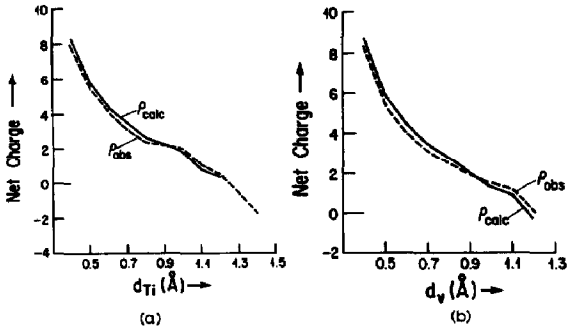

Fig. 6. Net charge vs. distance from the metal atom. (a) Ti_2O_3. (b) V_2O_3. Note the crossing of the observed and spherical atom (calc.) curves. From ref. 33, based on data from refs. 55 and 56.

metal atom, making assignment to a particular nucleus rather difficult. Whether or not the electrons are in the 4*s* orbital or on the ligand, they are still in approximately the same region in space.

One possible approach is to add up the electrons in the vicinity of the transition metal atom both for the experimental density and for the superposition of spherical atoms, the promolecule. This comparison will show whether charge migrates into or out of the region around the atom when the complex is formed.

We define a volume of integration which is polyhedral in shape, and determined by the geometry of the coordination sphere [32]. The position of the boundary planes depends on the relative size of the two adjacent atoms, R_A and R_B, such that the plane is located at $d = R_A l_{AB}/(R_A + R_B)$ from atom A, where l_{AB} is the bond length. For $Cr(CO)_6$ with its octahedral coordination this "Wigner–Seitz" cell becomes a particularly simple cube (Fig. 5a) of dimension depending on the choice of the ratio of the atomic radii.

The charge integrated over the chromium cell is plotted as a function of the position of the boundary plane in Fig. 5b. Independent of the boundary plane's position, the observed integrated density is evidently deficient (the metal more positive), compared with the calculated density based on the promolecule, but the difference is only about 0.5 e at reasonable values of d_{Cr}.

What is the best choice for the position of the boundary plane? One possibility would be to choose the boundary plane at the position where the atom in the promolecule would be neutral, i.e. at about 1.1 Å for $Cr(CO)_6$ (Fig. 5b). At this position the amount of carbon density in the volume of integration equals the amount of Cr density outside this volume. A prefer-

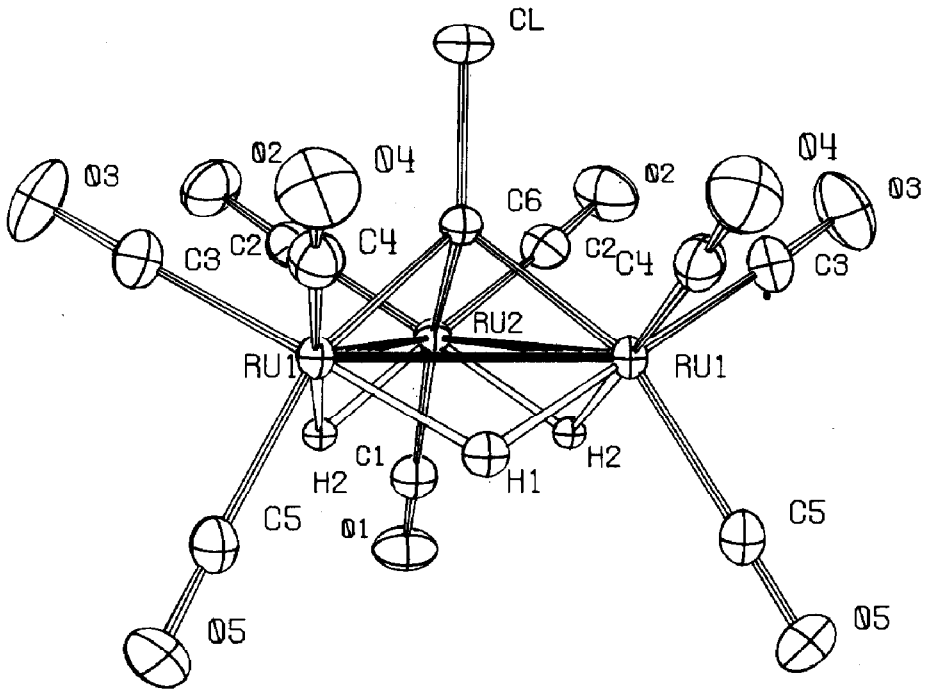

Fig. 7. Molecular structure of $Ru_3H_3CCl(CO)_9$. From ref. 34.

TABLE 4

Net populations and *d*-orbital occupancies in $Ru_3H_3(CO)_9CCl$

	Population	
	Theory [a]	Exp. [b]
Ru	0.484	1.16(5)
C_{apical}	−0.53	−0.81(4)
Cl	0.041	0.03(7)
H	−0.330	−0.18(3)
C	0.058	−0.55(4)
O	−0.059	0.31(4)

	d-Orbital occupancy [c] (%)		
	Theory [a]	Exp. [b]	Spherical atom
d_{z^2}	23.0	23.9	20
$d_{x^2-y^2}$	21.5	25.8	20
d_{xy}	20.0	16.2	20
d_{xz}	17.4	18.7	20
d_{yz}	18.2	15.3	20

[a] ref. 36. [b] ref. 34. (Numbers in parentheses represent experimental standard deviations.) [c] Definition of axes: x, in Ru_3 plane bisecting Ru–Ru–Ru angle; y, perpendicular to Ru_3 plane; z, perpendicular to x and y.

able alternative may be the positioning of the boundary plane such that the average density on its surface is a minimum. The average density on the surface equals the change of integrated electronic charge Q_e with volume V, dQ_e/dV, upon a change in d_{Cr}. It is plotted for $Cr(CO)_6$ as a function of d_{Cr} in Fig. 5c. This criterion leads to a boundary plane at about 0.8 Å from the chromium atom, i.e. less than half the Cr–C distance. As metal atom radii are generally perceived as being smaller than those of other atoms, this is a reasonable result. We note that at the latter *radius of best separation* and at the former *radius of non-bonded neutrality* the observed positive net charge on the transition metal atom in chromiumhexacarbonyl is small but positive. On the other hand a similar analysis of $Co_3CH(CO)_9$ gives a small negative charge for each of the three cobalt atoms [8], while in the corundum structures V_2O_3 and Ti_2O_3 the integrated charge curves of ρ_{obs} and ρ_{calc} cross at about 1.0 Å (Fig. 6), indicating an expansion of the metal atom density away from the atomic nucleus in these crystals [33], but a net charge which is dependent on the choice of atomic radii.

The charge integration method can be applied directly to the data, without the intervention of a model, but it requires a complete data set including all weak reflections, while the least-squares methods can be applied to partial data sets. It is of course possible to perform charge integration on the density calculated from the least-squares functions (the "model density"). But in this case the result is no longer model independent.

Finally, the fragment defined by the "zero flux boundary" surface introduced by Bader and coworkers [6], is a theoretically rigorous equivalent of the polyhedral volume of integration used here. The integral of ρ over a zero flux surface is a minimum with respect to any normal shift in the surface. This "virial partitioning" (it has been shown that each such fragment satisfies the virial theorem) has not yet been applied to molecules in crystals. The noise in experimental maps represents a potential problem, especially in the intermolecular region where the electron density is small. This difficulty can be circumvented, in principle, by integration over the model density based on the analytical functions from the least-squares refinement. Such an application, and its comparison with the result from theory, is highly desirable.

E. A STUDY OF A TRANSITION METAL HYDRIDE: $Ru_3H_3(CO)_9CCl$ [34]

The measurement of the electron distribution becomes progressively more difficult for heavier transition metal atoms, since the "bonding signal" in the valence electron density is small relative to the "background" respresented by the inner electrons' scattering. $Ru_3H_3(CO)_9CCl$, nonacarbonyl-μ_3-chloro-

methylidyne-tri-μ_2-hydrido-triangulotruthenium (Fig. 7), represents, in many ways, a test case of the limitations of experimental charge density studies. With three second-row transition metal atoms in close proximity, its suitability factor [35] for such studies is low. The hydrogen atoms' lone valence electron is hard to detect with X-ray methods, so the determination of its charge distribution is an undertaking requiring some optimism.

The initial X-ray study, done at 160 K on a small needle-shaped crystal (volume 0.0026 mm^3), showed large unexplained peaks near the ruthenium atoms, the exact location of which was dependent on the mode of X-ray data collection. For example, a data set collected with 90° rotation around the scattering vector produced similar ghost features but in very different positions. As this effect may be due to absorption correction errors, the study was repeated using a spherical crystal of 0.25 mm diameter.

From this second set of measurements at 100 K deformation density maps with lower background noise without extraneous peaks were obtained. The multipole formalism was applied to these measurements in a refinement including a parallel set of neutron data, which are of importance in fixing the position of the bridging hydrogen atoms.

The net atomic charges and the *d*-orbital population on the ruthenium atoms are listed in Table 4, in which a comparison is made with a Fenske–Hall type of calculation by Sherwood and Hall [36]. Since the calculation is approximate, and the experiment difficult, the discrepancies may be due to deficiencies in either method. But there are clear agreements: the hydrogen atoms are negative (theory −0.33 e, experiment −0.18(3) e), as may be expected for a hydride; the metal atoms positive (theory +0.48 e, experiment +1.16(5) e) and the apical carbon atom is negative (theory −0.53, experiment −0.81(4)). The *d*-orbital occupancies, when expressed as a percentage of total population, show a qualitative agreement: compared with the spherical atom the d_{z^2} and $d_{x^2-y^2}$ orbitals are favored, the d_{xz} and d_{yz} depopulated, while the d_{xy} orbital is depopulated according to the experiment and exactly average (i.e. 20%) according to the theory. The coordinate system, defined in Table 4, has its axes directed to the voids between the bonds. Thus the crystal field destabilization is again the dominant effect in this second-row transition metal atom.

The use of intense radiation at shorter wavelength as available from synchrotron sources may facilitate studies on heavier atom complexes if sufficiently stable beams can be obtained. With conventional sources we are close to the limit of applicability of the technique.

F. STUDIES OF METAL–METAL BONDING

Electron density studies of a number of metals and alloys have revealed little or no density accumulation between the metal atoms, in general

agreement with an itinerant electron model for bonding in metallic solids. In recent studies of chromium and vanadium metal [37], for example, no density is found in the deformation maps near the bond midpoints, but the atomic density appears somewhat distorted towards nearest neighbors [38]. The effect, however, is small and its analysis is complicated by the need to allow for anharmonic terms in the temperature factor formalism.

Aluminum-rich vanadium alloys are marked by the occurrence of aluminum polyhedra around a central vanadium atom. The V–Al bonds in these polyhedra are of unequal length. Several decades ago Black and Taylor noted that in many members of this group short V–Al bonds occurred in specific directions in the polyhedra, and suggested that these "anomalously" short bonds were indicative of chemical bonding [39]. A charge density study of several of the alloys [40] shows no evidence for strong bonding: within the accuracy of the experiment (0.05 $e\text{Å}^{-3}$) no density accumulation occurs.

As shown by Hall in his fragment deformation analysis of $Co_3CCl(CO)_9$ discussed above [9], the lack of density in metal–metal bonds in molecular complexes can at least in part be explained by a cancellation of electron withdrawal upon ligand attachment to the metal atom, and electron accumulation upon metal–metal bond formation. When the latter is unusually strong, as in the "super-short" Cr–Cr bond (1.879 Å at 74 K) in tetrakis(μ_2-hydroxy-6-methyl pyridine) dichromium, $[Cr_2(mhp)_4]$ [41], the overlap between the bonding hybrids becomes larger and a conventional bond peak is observed. The squared shape of this bond peak in the section through bond midpoint is different from the single, double and triple bond cross sections obtained for bonds between first-row atoms, and indicates a δ-contribution in addition to σ- and π-bonding. In $Cr_2(CH_3COO)_4$ in which the Cr–Cr length is 2.37 Å, no density is found on the bond axis, but a broad region of density accumulation is observed off the axis in the π- and δ-bonding regions [10]. In addition to the explanation given by Hall, Benard has attributed the weakness of the overlap features in this formally quadruple bond to the relatively long Cr–Cr bond length and to the very large contribution of excited configurations. These are non-bonding or antibonding in the metal–metal region, so that a formal bond order of considerably less than four is obtained. The contributions of excited configurations are much less pronounced in the isoelectronic dimolybdenum analog $Mo_2(H_3CCOO)_4$ for which some accumulation is found on the σ-bond axis, both experimentally and theoretically [42].

All these complexes have metal–metal bonds bridged by ligands: "through ligand" metal–metal bonding may be important in several instances. It is therefore of importance to analyze the electron distribution in a non-bridged complex. In manganese decacarbonyl, $Mn_2(CO)_{10}$, studied by Martin et al. [43] the bridging ligands are absent. Even though the Mn–Mn distance is

rather long (2.79 Å) there can be little doubt that the two $Mn(CO)_5$ fragments are held together by a metal–metal interaction. Nevertheless, the careful X-ray study by Martin et al. [43], and a theoretical calculation by Heyser [13] give atom deformation maps without density accumulation in the metal–metal bond region. The reason for this observation lies in the nature of the atom deformation map, as discussed earlier. If $Mn(CO)_5$ fragments are subtracted, a small density accumulation appears, as was the case in the study of $Co_3CCl(CO)_9$ by Hall and coworkers [9]. An analysis of the MO levels shows the HOMO to be the metal–metal bonding orbital, while the metal–metal antibonding orbital is the LUMO. For this $Mn_2(CO)_{10}$ complex a model based on the 18-electron rule gives the correct qualitative description of the bonding, with a single metal–metal bond. The following example is more complex, even though the 18-electron rule is still widely quoted to apply.

Dicobaltoctacarbonyl, $Co_2(CO)_8$, has often been considered a prototype for metal–metal bonding. The 18-electron rule in this diamagnetic complex can be satisfied by combining either two metal orbitals pointing along the metal–metal vector, leading to a straight bond, or two metal orbitals directed to the empty bridging site (compared with $Fe_2(CO)_9$), leading to a bent bond [44]. In an analogous molecular orbital scheme both bonding and antibonding states are filled for one of these two combinations, while the other is only half-filled, thus giving a net metal–metal bond.

The attractive simplicity of this explanation has stimulated both experimental [45] and theoretical [13] work. Both sets of studies lead to the conclusion that bonding in this complex is through the ligands, rather than by direct metal to metal interaction. The CO deformation density which is cylindrically symmetric in the isolated ligand shows pronounced asymmetry at the carbon "lone-pair" position, with an elongation in the Co–C–Co

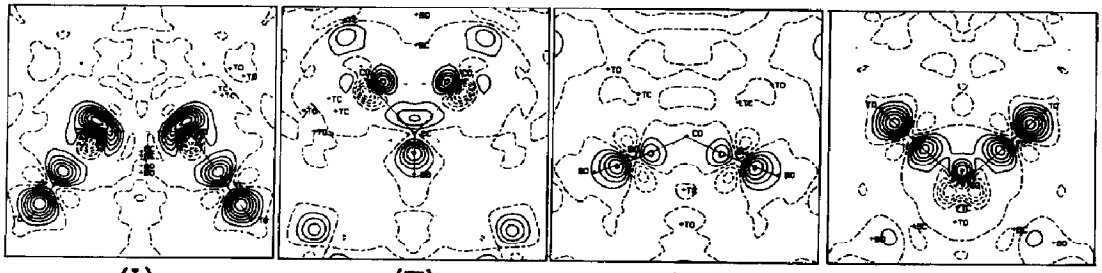

Fig. 8. Electron deformation density in $Co_2(CO)_8$, according to aspherical atom (multipole) refinement. Contours at 0.1 eÅ^{-3}. Zero and negative contours broken. (I) in plane containing two cobalt atoms and two terminal carbonyl groups; (II) in plane containing two cobalt atoms and one bridging carbonyl group; (III) in plane through two bridging carbonyl groups; (IV) in plane through two terminal carbonyl groups. From ref. 45.

plane (Fig. 8). This is exactly what is predicted by the SCF calculations with X-α exchange, which indicate the stability of the dimer to be due to interaction of the metal e_g' orbitals with the $2\pi_{\parallel}$ orbital of the bridging carbonyl, leading to three-center bonds through the bridging ligands. The metal orbitals pointing towards the other metal atom are all of low energy and combine into doubly occupied MO's, thus producing no net bonding, in contradiction to the popular 18-electron rule explanation.

The *d*-orbital occupancies from the theoretical and experimental analyses are in quite reasonable agreement. When experimental populations are expressed in a pseudo C_{4v} system with its *z*-axis along a terminal CO ligand [45], and *x* and *y* in the directions of the other terminal and bridging ligands, the crystal field splitting becomes evident. It is the dominant effect with d_{z^2} and $d_{x^2-y^2}$ being depopulated relative to the other orbitals.

G. THE NATURE OF METAL–LIGAND BONDING

It is well known that the molecular and electronic structure of ligand molecules is affected by bonding to metal atoms. Changes in spectroscopic properties and three-dimensional structure have been extensively documented and are of course relevant to chemical behavior in homogeneous and heterogeneous catalysis. The changes in the ligand charge distribution are measurable and have been obtained for $Cr(CO)_6$, $Co_3CH(CO)_9$ and $Co_2(CO)_8$. In particular for the C–O ligand in chromiumhexacarbonyl and the CH ligand in nonacarbonyl-μ_3-methylidyne-triangulocobalt (Figs. 2a, c) the σ-donation, π-back-donation model due to Dewar and Chatt [21] has been confirmed by the ligand-deformation maps.

Even though the effect of covalency is observed directly through the population of the crystal-field destabilized orbitals as described above, the overlap density in the metal–ligand bond is not observed, unlike the density accumulations found in, for example, every bond of the porphyrin skeleton of metalloporphyrins. This is a result of the small value of the overlap between the metal and ligand orbitals. However, in the spin densities which can be observed at very low temperatures in paramagnetic complexes, overlap effects are stronger and easily visible (Fig. 9).

The three-electron case is illustrative. It can be discussed within the spin-restricted MO formalism [5,46]. Starting with a metal orbital ϕ and a ligand orbital χ, which in general will be a symmetry-adapted combination of orbitals on several ligand atoms, the bonding and antibonding orbitals may, respectively, be written as:

$$\psi_B = [1 + 2\gamma S + \gamma^2]^{-1/2}(\chi + \gamma\phi)$$

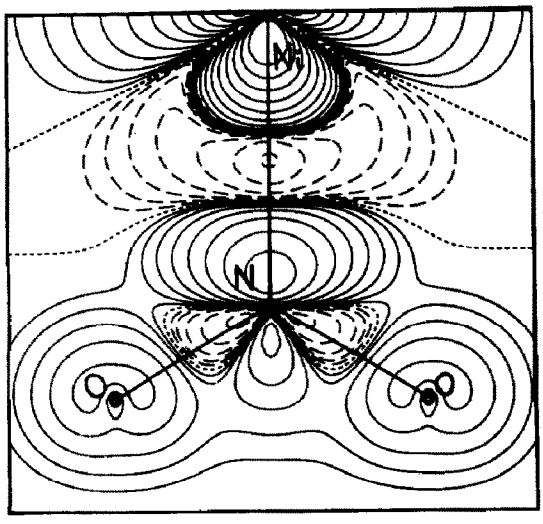

(A)

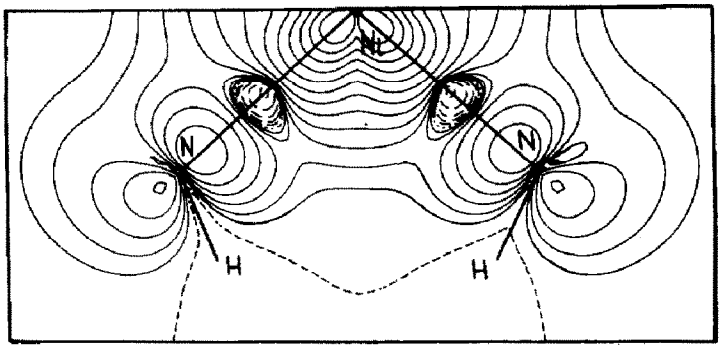

(B)

Fig. 9. Spin density in $Ni(NH_3)_4(NO_2^-)_2$ according to aspherical atom refinement. Logarithmic contours, lowest 0.00164 spin $Å^{-3}$, highest 3.4 spin $Å^{-3}$; increasing by a factor 2. Positive, solid contours; negative, dashed contours; zero dotted. (a) In plane containing Ni and NO_2. (b) In plane containing Ni and nitrogens of two NH_3 ligands. From ref. 48.

and

$$\psi_{AB} = [1 - 2\lambda S + \lambda^2]^{-1/2}(\phi - \lambda\chi)$$

where S is the overlap integral $\langle\phi|\chi\rangle$ and λ is given by the orthogonality condition $\langle\chi_B|\chi_{AB}\rangle = 0$, which leads to $\lambda = \gamma + S$. For the charge density ρ and the spin density s this leads to:

$$\rho_{\text{overlap}} = 2(\gamma - S)\phi\chi$$

and

$$s_{\text{overlap}} = -2(\gamma + S)\phi\chi$$

Since γ and S are positive, the effect of the overlap density on the spin distribution s should be much more pronounced. This is confirmed by experiment. In one of very few studies in which charge and spin densities have been combined [47,48] Figgis and coworkers found a significant negative spin density in the Ni–N bonds in $Ni(NH_3)_4(NO_2)_2$ (Fig. 9), but no pronounced charge density accumulation at bond midpoints. From the spin density results only, values for γ of about 0.5 and 0.6 can be derived for the $Ni–NH_3$ and $Ni–NO_2$ bonds respectively.

The simultaneous interpretation of the two sets of data leads to a more complete description of the bonding. Coppens et al. [49] combined their data on cobalttetraphenylporphyrin (CoTPP) with spin density results by Varghese and Mason [50] and Williams et al. [51] on cobaltphthalocyanine (CoPc), using the similarity of the tetraphenylporphyrin and phthalocyanine ligands which are identical in the vicinity of the metal atom. The agreement between the populations of *d*-orbitals not or very little affected by bonding is striking (Table 5).

For the $d_{x^2-y^2}$ orbital, which points directly to the ligand nitrogen atoms and is affected by bonding, the spin density result is $\rho\uparrow - \rho\downarrow = -0.21$ e, while $\rho\uparrow + \rho\downarrow$ from the charge density is 0.83 e. Using the relations $\rho\uparrow = (\rho_{\text{charge}} + \rho_{\text{spin}})/2$ and $\rho\downarrow = (\rho_{\text{charge}} - \rho_{\text{spin}})/2$ we get $\rho\uparrow = 0.3$ and $\rho\downarrow = 0.5$ e. This indicates that 0.6 of the atomic electrons are to be accounted for by contributions of excited configurations with unpaired electron density in $d_{x^2-y^2}$.

If ψ_B is doubly occupied and we neglect the overlap term in the charge

TABLE 5

Charge and spin density populations in CoTPP and CoPc (from ref. 49)

	X-ray		Neutron		
	Charge CoTPP	Spin CoPc	Charge [a] CoPc	$\rho\uparrow$	$\rho\downarrow$
$b_1(d_{x^2-y^2})$	0.83(20)	−0.21(10)	0.21	0.3	0.5
$a_1(d_{z^2})$	0.92(20)	0.79(12)	1.21	0.8_6	0.0_6
$b_2(d_{xy})$	1.64(20)	0.40(10)	1.60	1.0	0.6
$e(d_{xz}, d_{yz})$	3.62(20)	0.34(20)	3.66	2.0	1.6
4*s*	–	−0.14(16)	0.14 or 1.86	–	0.14

[a] Charge population obtained from spin population by assuming positive spin density to be due to hole in d^2 occupancy of each of the orbitals, except for the less than half filled b_1 orbital.

TABLE 6

Charge and spin density populations in *trans*-$Ni(NH_3)_4(NO_2)_2$ (from refs. 51 and 52) (z-axis pointing towards NO_2 ligands; x and y axes bisecting NH_3–Ni–NH_3 angles.)

	Charge	Spin
$3d_{xy}$	1.28(7)	0.87(7)
$3d_{yz}$	1.80(6)	0.04(4)
$3d_{xz}$	1.31(6)	−0.02(7)
$3d_{z^2}$	1.36(8)	0.84(7)
$3d_{x^2-y^2}$	1.84(7)	−0.05(6)
$4p_x$	1.59(20)	0.17(6)
$4p_y$	0.09(20)	0.07(6)
$4p_z$	−0.19(20)	−0.14(7)

density, which is small, the $d_{x^2-y^2}$ part of the population of the doubly occupied orbital ψ_B is equal to $2(1+\gamma^2)^{-1}$. Equating this to the experimental value of 0.6 e leads to $\gamma = 0.65$. In other words, the bonding orbital has predominant ligand character, in agreement with the σ-donation concept.

In the crystal field approximation for the d^7 Co^{2+} ion, the $d_{x^2-y^2}$ bonding orbital is not occupied, while all other orbitals contain at least one electron. In the d^8 Ni^{2+} ion in *trans*-$Ni(NH_3)_4(NO_2)_2$ the d_{z^2} and d_{xy} orbitals (note the non-conventional choice of x and y axes which are pointing towards the NO_2 and NH_3 ligands respectively) are both singly occupied in the crystal field approximation. σ-Donation from the ligands leads to a total occupancy larger than one and a net spin which is ↑ (i.e. majority spin) and is smaller than one, as is indeed found experimentally (Table 6), and predicted with more rigorous arguments than presented here [46].

Using the reasoning applied above for the Co complex, we find for the $Ni(NH_3)_4(NO_2)_2$ d_{xy} and d_{z^2} orbitals, $\gamma_{NH_3} = 0.5$ and $\gamma_{NO_2^-} = 0.6$, in excellent agreement with values derived by Figgis et al. from the spin density alone. As noted by these authors the slightly larger covalency of NO_2^- bonding is in agreement with the spectrochemical series. In the $CoCl_4^{2-}$ ion the covalency coefficient is much smaller [52], again in agreement with accepted chemical concepts.

The combination of X-ray and polarized neutron data on paramagnetic complexes is a particularly powerful probe of electronic structure. A comprehensive treatment of both sets of data has not yet been achieved, but further studies may be expected in the near future.

ACKNOWLEDGEMENTS

Support by the National Science Foundation (CHE7905897) and the National Institute of Health (HL2388404A1) is gratefully acknowledged.

The author thanks Prof. B.N. Figgis for his comments on an earlier version of this review.

REFERENCES

1 P. Coppens, Top. Curr. Phys., 6 (1977) 71.
2 F.L. Hirshfeld (Ed.), Isr. J. Chem., 16(2-3) (1977).
3 P.J. Becker (Ed.), Electron and Magnetization Densities in Molecules and Crystals, NATO Adv. Study Ser. B48 (1979).
4 P. Coppens and M.B. Hall (Eds.), Electron Densities and the Chemical Bond, Plenum, New York, 1982.
5 B.C. Tofield, Struct. Bonding, 21 (1975) 1–87.
6 R.F.W. Bader, Y. Tal, S.G. Anderson and T.T. Nguyen Dang, Isr. J. Chem., 19 (1980) 8. R.F.W. Bader, P.J. MacDougall and D.C.H. Lau, J. Am. Chem. Soc., 106 (1984) 1594 and references therein.
7 P. Coppens in P. Coppens and M.B. Hall (Eds.), Electron Densities and the Chemical Bond, Plenum, New York, 1982, p. 61.
8 P.C.W. Leung, Thesis, State University of New York at Buffalo, 1982.
9 M.B. Hall in P. Coppens and M.B. Hall (Eds.), Electron Densities and the Chemical Bond, Plenum, New York, 1982, p. 205. P.T. Chesky and M.B. Hall, Inorg. Chem., 20 (1981) 4419.
10 M. Benard, P. Coppens, M.L. DeLucia and E.D. Stevens, Inorg. Chem., 19 (1980) 1924.
11 A. Mitschler, B. Rees and M.S. Lehmann, J. Am. Chem. Soc., 100 (1980) 3390.
12 M. Benard in P. Coppens and M.B. Hall (Eds.), Electron Densities and the Chemical Bond, Plenum, New York, 1982, p. 221.
13 W. Heyser, Thesis, Free University, Amsterdam. W. Heyser, E.J. Baerends and P. Ros, Faraday Symp. Chem. Soc., 14 (1980) 211.
14 P. Coppens, T.N. Guru Row, P.C.W. Leung, E.D. Stevens, P.J. Becker and Y.W. Yang, Acta Crystallogr., Sect. A, 35 (1979) 63.
15 F.L. Hirshfeld, in ref. 2, p. 226.
16 N.K. Hansen and P. Coppens, Acta Crystallogr., Sect. A, 34 (1978) 909.
17 E.V. Condon and G.H. Shortley, Theory of Atomic Spectra, Cambridge University Press, Cambridge, 1957.
18 B. Rees and A. Mitschler, J. Am. Chem. Soc., 98 (1976) 7918.
19 M. Iwata and Y. Saito, Acta Crystallogr., Sect. B, 29 (1973) 822.
20 M. Iwata, Acta Crystallogr., Sect. B, 33 (1977) 59.
21 M.J.S. Dewar, Bull. Soc. Chim. Fr., 18 (1951) C71. J. Chatt and L.A. Duncanson, J. Chem. Soc., (1953) 2939.
22 E.D. Stevens, M.L. DeLucia and P. Coppens, Inorg. Chem., 19 (1980) 813.
23 N. Miyata, K. Tanaka and F. Marumo, Acta Crystallogr., Sect. B, 39 (1983) 561.
24 P. Coppens, L. Li and N.J. Zhu, J. Am. Chem. Soc., 105 (1983) 6173. P. Coppens and L. Li, J. Chem. Phys., 81 (1984) 1983.
25 K. Tanaka, J. Landrum, L. Li and P. Coppens, in preparation.
26 E.D. Stevens, J. Rys and P. Coppens, J. Am. Chem. Soc., 100 (1978) 2324.
27 J.F. Griffin and P. Coppens, J. Am. Chem. Soc., 97 (1975) 3496.
28 W. Bats, P. Coppens and T.F. Koetzle, Acta Crystallogr., Sect. B, 33 (1977) 37.
29 F. Baert, P. Coppens, E.D. Stevens and L. Devos, Acta Crystallogr., Sect. A, 38 (1982) 143.

30 D.A. Pearlman and S.H. Kim, Biopolymers, in press.
31 A. Holladay, P.C.W. Leung and P. Coppens, Acta Crystallogr., Sect. A, 39 (1983) 440.
32 P. Coppens and T.N. Guru Row, Ann. N.Y. Acad. Sci., 313 (1978) 244.
33 A. Holladay, Thesis, State University of New York at Buffalo, 1983.
34 N.J. Zhu, T.F. Koetzle and P. Coppens, unpublished results. N.J. Zhu, C. Lecomte, P. Coppens and J.B. Keister, Acta Crystallogr., Sect. B, 38 (1982) 1286.
35 E.D. Stevens and P. Coppens, Acta Crystallogr., Sect. A, 32 (1976) 915.
36 D.E. Sherwood and M.B. Hall, Organometallics, 1 (1982) 1519.
37 S. Ohba, S. Sato and Y. Saito, Acta Crystallogr., Sect. A, 37 (1981) 697.
38 In the superconducting alloy V_3Si, the V–V distances are appreciably shorter than in vanadium metal. In this material electron density accumulation between metal atoms has been observed. J.L. Staudenmann, P. Coppens and J. Muller, Solid State Commun., 19 (1976) 29.
39 P.J. Black and W.H.T. Taylor, Rev. Mod. Phys., 30 (1958) 55.
40 A. Kontio, Thesis, University of Helsinki, 1984.
41 A. Mitschler, B. Rees, R. Wiest and M. Benard, J. Am. Chem. Soc., 104 (1982) 7501.
42 K. Hino, Y. Saito and M. Benard, Acta Crystallogr., Sect. B, 37 (1981) 2164.
43 M. Martin, B. Rees and A. Mitschler, Acta Crystallogr., Sect. B, 38 (1982) 6.
44 G.G. Sumner, H.P. Klug and L.E. Alexander, Acta Crystallogr., 17 (1964) 732. P.S. Braterman, Struct. Bonding (Berlin), 10 (1983) 57.
45 P.C.W. Leung and P. Coppens, Acta Crystallogr., Sect. B, 39 (1983) 535.
46 P.J. Becker and P. Coppens, Acta Crystallogr., Sect. A, in press.
47 B.N. Figgis, P.A. Reynolds and S. Wright, J. Am. Chem. Soc., 105 (1983) 434.
48 B.N. Figgis, P.A. Reynolds and R. Mason, J. Am. Chem. Soc., 105 (1983) 440.
49 P. Coppens, A. Holladay and E.D. Stevens, J. Am. Chem. Soc., 104 (1982) 3546.
50 J.N. Varghese and R. Mason, Proc. R. Soc. London, Ser. A, 372 (1980) 1.
51 G.A. Williams, B.N. Figgis and R. Mason, J. Am. Chem. Soc., 103 (1981) 734.
52 G.S. Chandler, B.N. Figgis, R.A. Phillips, P.A. Reynolds, R. Mason and G.A. Williams, Proc. R. Soc. London, Ser. A, 384 (1982) 31.
53 M. Sano, H. Kashiwagi and H. Yamatera, Inorg. Chem., 21 (1982) 3837.
54 M. Sano, H. Yamatera and Y. Hatano, Bull. Chem. Soc. Jpn., 54 (1981) 2898.
55 M.G. Vincent, K. Yvon, A. Gruettner and J. Ashkenazi, Acta Crystallogr., Sect. A, 36 (1980) 803.
56 M.G. Vincent, K. Yvon and J. Ashkenazi, Acta Crystallogr., Sect. A, 36 (1980) 808.